Studying the Milky Way pulsar population with cosmic-ray leptons

Ilias Cholis,[1,2] Tanvi Karwal,[2] and Marc Kamionkowski[2]
[1]Department of Physics, Oakland University, Rochester, Michigan 48309 USA
[2]Department of Physics and Astronomy, The Johns Hopkins University, Baltimore, Maryland 21218, USA

(Received 24 July 2018; published 12 September 2018)

Recent measurements of cosmic-ray electron and positron spectra at energies from a GeV to 5 TeV, as well as radio, x-ray and a wide range of gamma-ray observations of pulsar-wind nebulae, indicate that pulsars are significant sources of high-energy cosmic-ray electrons and positrons. Here, we calculate the local cosmic-ray $e^{\pm}$ energy spectra from pulsars taking into account models for (a) the distribution of the pulsars spin-down properties, (b) the cosmic-ray source spectra, and (c) the physics of cosmic-ray propagation. We then use the measured cosmic-ray fluxes from *AMS-02*, *CALET* and *DAMPE* to constrain the space of pulsar and cosmic-ray-propagation models and, in particular, local cosmic-ray diffusion and energy losses, the pulsars' energy-loss time dependence, and the injected $e^{\pm}$ spectra. We find that the lower estimates for the local $e^{\pm}$ energy losses are inconsistent with the data. We also find that pulsar braking indexes of 2.5 or less for sources with ages more than 10 kyr are strongly disfavored. Moreover, the cosmic-ray data are consistent with a wide range of assumptions on the $e^{\pm}$ injection spectral properties and on the distribution of initial spin-down powers. Above a TeV in energy, we find that pulsars can easily explain the observed change in the $e^{+}+e^{-}$ spectral slope. These conclusions are valid as long as pulsars contribute $\gtrsim$10% of the observed cosmic-ray $e^{\pm}$ at energies $\gtrsim$100 GeV.

DOI: 10.1103/PhysRevD.98.063008

I. INTRODUCTION

Observations of electromagnetic radiation from pulsars and their surrounding environment, including the pulsar wind nebulae (PWNe), from radio wavelengths to γ rays [1–4], suggest that pulsars are a significant source of high-energy cosmic-ray electrons and positrons. In particular, HAWC [5,6] and Milagro [7] both recently observed γ-ray halos at energies of 10 TeV and above around Geminga and Monogem, two nearby pulsars. These observations are well accounted for by the escape of cosmic-ray $e^{\pm}$ from the relevant PWNe which then produce the observed gamma rays via inverse-Compton scattering (ICS) of background light within a volume of $\sim 10^3$ pc^3 around the pulsar [6,8]. Follow-up observations will soon address remaining uncertainties in the diffusion and energy losses of these leptons in the interstellar medium (ISM) and the possible effects of convective winds around Geminga and Monogem. Still, current data already indicate that pulsars and PWNe can accelerate significant fluxes of $e^{\pm}$ with potential implications for future pulsar searches [9].

Cosmic-ray electrons are also thought to be shock-accelerated to energies between a keV and $\sim$100 TeV in supernova remnants. At low energies, cosmic-ray electrons and positrons may also be produced from inelastic collisions of cosmic-ray nuclei with nuclei in the ISM. These are commonly known as secondary electrons and positrons, and numerical codes calculating their spectra have been developed e.g., in Refs. [10–14].

There is roughly one pulsar born in the Galaxy per century [15–19]. Electrons and positrons suffer from energy losses due to synchrotron radiation and ICS off the cosmic microwave background (CMB) and infrared/optical starlight as they diffusively propagate through the ISM. The interplay of diffusion and energy losses gives a rough maximum energy $E_{\rm max} \sim 100\ {\rm GeV}(R/2\ {\rm kpc})^{-2}$ [20] for $e^{\pm}$ that survive at a distance R from their source. Thus, fewer sources can contribute to the $e^{\pm}$ flux observed at higher energies at any given location. A rate of one pulsar per century suggests that only a few dozen pulsars contribute to the $e^{\pm}$ flux above 500 GeV. The discreteness of the source population can result in spectral features in the $e^{\pm}$ energy spectra [21,22] that might be sought, e.g., with a fluctuation analysis of the energy spectra [20].

The aim of this paper is to use existing measurements of the $e^{\pm}$ energy spectra to constrain the properties of the pulsar population within a few kpc from the Earth. We do so by simulating a large number of realizations of pulsar distributions for an array of models of the astrophysical conditions impacting the cosmic-ray spectra from pulsars. We first simulate the spatial distribution of pulsars. Then, for each simulation, we calculate the local CR $e^{\pm}$ spectrum for an array of different assumptions on the injected $e^{\pm}$ spectra and cosmic-ray propagation conditions. By requiring the local cosmic-ray $e^{\pm}$ energy spectra to agree with measurements, we exclude over three quarters of the models and find several conclusions that can be drawn

even after marginalizing over the model uncertainties. These conclusions include that braking indexes of 2.5 or less, that have been observed for some very young pulsars, are excluded by CR data that rely on the characteristics of sources older than 10 kyr. Furthermore, we show that if the local ISM conditions result in low energy losses, then pulsars can not explain the data. If such conditions are avoided, pulsars can explain the CR data with the positron fraction above 300 GeV being either flat, increasing or decreasing with energy. Additionally, a total $e^+ + e^-$ spectrum with a softer slope is a typical expectation of pulsar sources if very young sources such as Vela are still subdominant contributors in the local $e^{\pm}$.

This paper is organized as follows: In Sec. II, we describe the simulations, enumerate the assumptions made, and clarify the astrophysical uncertainties involved in the simulations. In Sec. III, we present the simulations that are allowed by the data. We discuss first our fits to the *AMS-02* positron fraction ($e^+/(e^+ + e^-)$) measurement. Then we show the impact of adding into our analysis $e^+ + e^-$ fluxes from *CALET* and *DAMPE*. We conclude and discuss future directions in Sec. IV.

II. METHOD

A. Cosmic-ray data

We use the published *AMS-02* data from Ref. [23] collected over a period of 2.5 years. We ignore the measurement associated with energies below 5 GeV since at these energies the spectra are strongly affected by the solar wind and because pulsars contribute marginally. We focus instead on the measurement above 5 GeV and up to 500 GeV. In addition, we consider the impact of a turnover in the positron fraction above 500 GeV, as suggested recently [24]. Since this is not a published measurement, we indicate the impact if the result stands, but also provide results without it. In addition, we use the 1.5 years of spectral measurements of the combined $e^+ + e^-$ CR flux, from 25 GeV up to 5 TeV, by *DAMPE* [25,26] as well as the same spectral measurements by *CALET* [27–29] at energies between 10 GeV and 5 TeV, taken over an extension of two years. We note that the measurements by *DAMPE* and *CALET* are in statistical tension with each other and thus avoid fitting to both data sets. Instead, we only check for consistency between the *AMS-02* positron fraction and each of these electron- plus-positron spectra separately.

B. Studying the pulsar population

The contribution of local pulsars to the measured CR spectra is influenced by uncertainties. We model these uncertainties by producing astrophysical realizations spanning the relevant multidimensional parameter space in a discrete manner. We call these unique points on this space "pulsar astrophysical realizations" or just "simulations." An example of four such pulsar astrophysical realizations is shown in Fig. 1. The current data show that the positron fraction rises monotonically from 7 to ∼300 GeV. We show several simulations that fit the data over the range that it is measured. These fitted simulations show that the spectrum can either continue to rise to a value $\gtrsim$0.20 at an energy of a TeV or flatten to a value of $\simeq$0.16, or even drop to $\simeq$0.1 at that energy. *AMS-02* will have the sensitivity to eventually observe such values of the positron fraction. Moreover, different astrophysical realizations can predict a pulsar spectrum that is inherently smooth and featureless or one that has detectable features [20].

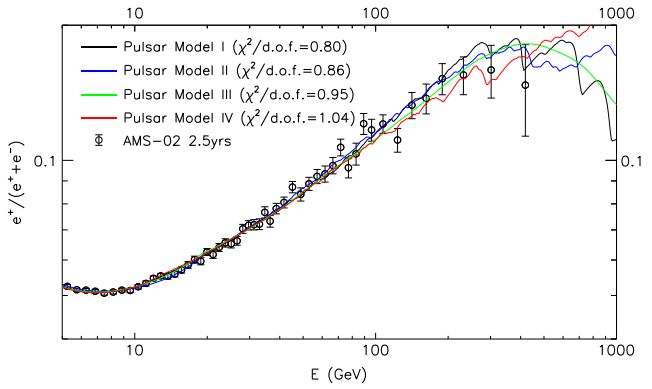

FIG. 1. Four different pulsar astrophysical realizations. The predicted positron-fraction spectrum, which is observed to increase from 7 to ∼300 GeV, can either drop at higher energies (model I, in black line), flatten out (model II, in blue line), or keep rising up to a TeV (model IV, in red line). Also, depending on the exact ISM assumptions (see text for details and Fig. 3), it can be smooth (green line) or have features associated with individual pulsars whose presence can potentially be detected [20].

1. Neutron star birth distribution

As discussed in the Introduction, the cosmic-ray $e^{\pm}$ observed locally come from sources within a radius R from us where, as described in the Introduction, that radius is smaller at higher energies. Thus, the observed cosmic-ray $e^{\pm}$ flux is sensitive to the spatial distribution and birth rate within this volume. The birth rate and spatial distribution of pulsars within the Milky have been subjects of extensive work [17,18,30,31]. Yet there are great uncertainties in both, given the lack of a complete pulsar survey of the sky at radio wavelengths. Moreover, the pulsars' radio emission is highly anisotropic, beamed with an opening angle spanning about one tenth of the pulsars' 4π steradians. In fact, observations suggest that this ratio (typically referred to as the beaming fraction) is time dependent, being larger at the earlier stages of the pulsar's evolution (as high as $\simeq$50% during its first 10 kyr) and gradually decreasing [32]. At gamma-ray wavelengths, the surveys do span the entirety of the sky but are sensitive only to the brightest sources, i.e., the most powerful, younger, and nearby members of the pulsar population.

The Milky Way pulsar birth rate has been estimated to be 1.4 ± 0.2 per century in Ref. [18], with alternative estimates that range between one and four per century at one σ [16,17,19] and even as high as $\simeq 8$ per century [15]. In our analysis, the pulsar birth rate is degenerate with the fraction of spin-down power that goes to high energy $e^{\pm}$ and thus for simplicity we choose it to be one per century. The spatial distribution of pulsars at birth is expected to follow the stellar distribution in the Milky Way's spiral arms. It has been modeled in Refs. [17,18,30] based on the Parkes multibeam survey at 1.4 GHz [33]. We generate simulations of Milky Way pulsar populations. To generate simulations of Milky Way pulsar populations, we follow both the parametrization of Refs. [30] and [18] taking the latter as the canonical distribution. More precisely, for the distribution of pulsars in galactocentric distance r, we use the radial density profile,

$$\rho(r; B, C) = A\left(\frac{r}{R_\odot}\right)^B \exp\left(-C\left[\frac{r - R_\odot}{R_\odot}\right]\right), \quad (1)$$

where $B = 1.9$, $C = 5.0$, $R_\odot = 8.5$ kpc, and A is normalized to a pulsar birth rate of one per century. Furthermore, in our generated simulations, pulsars have a distance z away from the disk that follows a Laplace distribution with a scale height of 50 pc and mean of 0 pc, in accordance with Ref. [17]. Finally, we do not try to simulate the spiral arms of the Galaxy, but simply assume a uniform distribution in galactocentric angle.

2. Neutron-star spin-down

Neutron stars (NSs) are born from the core collapse of massive stars in the range of 8–25 $M_\odot$. Given their violent birth combined with supernova explosions not being perfectly spherically symmetric, neutron stars have large three-dimensional kick velocities (e.g., Ref. [34] find kick velocity to be 400 ± 40 km/s) and also large ($\sim 10^{49}$ erg) initial rotational energies. They also have strong magnetic fields due to the contraction of the initial core, with large uncertainties in the magnetic-field strengths due to magnetohydrodynamic instabilities formed in the early stages of the NS birth. The strength of the initial magnetic fields at the poles ranges between $\sim 10^{12}$–10^{15} G. These rapidly rotating strong magnets will suffer the loss of rotational energy with initial spin-down powers that may also span orders of magnitude given the large uncertainties in the initial magnetic fields and rotational frequencies. This spin-down power evolves with time as

$$\dot{E}(t) = \dot{E}_0\left(1 + \frac{t}{\tau_0}\right)^{-\frac{\kappa+1}{\kappa-1}}. \quad (2)$$

Here, E_0 is the initial rotational energy (i.e., $E_0 = 1/2 I_0 \Omega_0^2$, with I_0 the neutron-star moment of inertia and Ω_0 its initial angular frequency),

$$\tau_0 = \frac{\dot{\Omega}}{(\kappa - 1)\Omega}\left[1 - \left(\frac{\Omega}{\Omega_0}\right)^{\kappa - 1}\right] \quad (3)$$

is the characteristic time scale, or age, of a pulsar, and κ is the braking index describing the time evolution of the neutron stars' angular frequency Ω through $\dot{\Omega} \propto \Omega^\kappa$. Setting $\kappa = 3$ describes the spin-down due to magnetic-dipole radiation [35]. Measurement of κ demands knowledge of Ω, $\dot{\Omega}$ and $\ddot{\Omega}$ ($\kappa \equiv \ddot{\Omega}\Omega/\dot{\Omega}^2$). This biases the measurement toward young pulsars where $\ddot{\Omega}$ is not too small to measure, and young pulsars may not be characteristic of the general distribution. Typical observed values give $\kappa \lesssim 3$ [36–44], but there are also recent measurements of young pulsars with higher braking-index values [45]. Moreover, the pulsar braking index may evolve with time [32,35] depending on the specific properties of the pulsar [46].

Given these uncertainties, our simulations test three different choices, $\kappa = 2.5$, 3.0, and 3.5 for the braking index. For each choice, we also choose a value for the characteristic spin-down timescale τ_0. Finally, we account for pulsars not having a universal initial spin-down power given the wide ranges of observed magnetic fields for young pulsars ($\sim 10^{12}$–$10^{14.5}$ G). We simulate pulsars with an initial spin-down power $\dot{E}_0$ given by

$$\dot{E}_0 = 10^x \text{ erg/s} = 10^{x_{\text{cutoff}} - y} \text{ erg/s}, \quad \text{with}$$
$$f(y) = \frac{\text{Exp}\left\{-\frac{[-\mu_y + \ln(y)]^2}{2\sigma_y^2}\right\}}{\sqrt{2\pi} y \sigma_y}. \quad (4)$$

The values for x_{cutoff} and μ_y are constrained by radio observations of rotation periods and modeled surface magnetic fields of Myr old pulsars [17]. Moreover observation of the Crab pulsar at $\simeq 1$ kyr imposes a hard cutoff on observed spin-down power of pulsars larger than $10^{38.7}$ erg/s [47,48]. In our simulations we take $\sigma_y = [0.25, 0.36, 0.5, 0.75]$. Those observational constraints result in pulsars with τ_0 values as small as 0.6 kyr for $\kappa = 2.5$ and as large as 30 kyr for $\kappa = 3.5$, with typical values of 6–10 kyr for breaking index of 3.0. In Fig. 2, we show normalized histograms of $\dot{E}$ for each value of σ_y for simulations that are allowed by the data.

We allow for a wide range of assumptions regarding the true underlying current period of pulsars with ages ≤ 10 Myr, as well as their surface magnetic fields. Since we rely on observations of pulsars with ages of order 10^5–10^7 years, we probe predominantly that population and not the spin-down conditions in the very early stages. We then use the CR measurements to constrain the birth properties of the pulsar population.

We also note that neutron-star kick velocities of ~ 100 km/s result in a displacement of ~ 100 pc of the NSs from their birth location within 1 Myr, but only a few

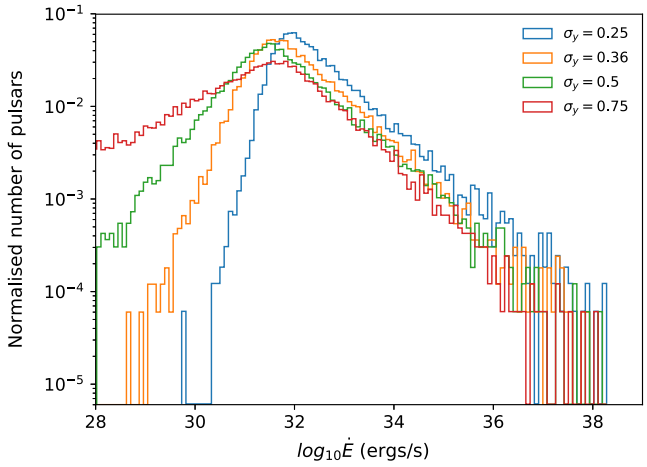

FIG. 2. Shown here are normalized histograms of pulsar luminosities from various realizations. This is not their birth luminosity, but the luminosity evolved to today using Eq. (2). All simulations shown have a braking index of $\kappa = 3.0$. The surface magnetic fields as well as periods of pulsars with distributions in orange and red are in good agreement with results shown in Fig. 6 of Ref. [17]. For the blue histogram, the surface magnetic fields of simulated pulsars and for the green, their periods agree well with Ref. [17]. At high luminosities one can notice the Poisson fluctuations that arise in each individual simulation. All distributions shown are associated with models that are allowed by the data.

pc in their first ∼10 kyr ($\simeq\tau_0$) that is relevant for our work. We thus take their distribution in space to be their distribution at birth.

3. Injection properties of cosmic-ray $e^{\pm}$

From radio and microwave observations of synchrotron radiation close to the NS magnetic poles and of inverse Compton scattering in gamma rays further away from the NS, we know that $e^{\pm}$ pairs are produced and get accelerated inside the pulsar magnetospheres (up to distance scales $O(10^4$–$10^5)$ km) [49–63]. In addition, $e^{\pm}$ can get accelerated outside the pulsar magnetosphere before or at the PWN termination shock that typically extends out to ∼pc distances from the NS [62,64–71]. In fact, there is evidence for the presence of ∼100 TeV $e^{\pm}$ at even larger distances, of ≃10 pc, from HAWC observations of gamma rays at ∼10 TeV from the pulsars Geminga and Monogem [5,6]. All these observations suggest that pulsars are environments that are rich in high-energy $e^{\pm}$, a fraction of which may escape into the ISM as cosmic rays.

Following Ref. [21], we assume that each pulsar is a point source of CR $e^{\pm}$ described by a source term,

$$Q(E,\vec{x},t) = \frac{dN}{dE}\delta(\vec{x})\left(1+\frac{t}{\tau_0}\right)^{\frac{\kappa+1}{\kappa-1}}, \quad \text{with}$$
$$\frac{dN}{dE} = Q_0\left(\frac{E}{1\ \text{GeV}}\right)^{-n}\text{Exp}\left\{-\frac{E}{E_{\text{cut}}}\right\}, \tag{5}$$

the CR energy density from a given pulsar. Here, $\delta(\vec{x})$ is a Dirac delta function localized at the pulsar position, and the normalization of Q_0 is such that [21],

$$\iiint dE\, d\vec{x} dt Q(E,\vec{x},t) = \eta W_0, \tag{6}$$

where η is the fraction of the rotational energy W_0 that has already been lost through CR $e^{\pm}$ injected into the ISM. This gives,

$$Q_0 = \frac{E_{\text{cut}}^{2-n}}{\Gamma(2-n)}\frac{2}{(\kappa-1)\tau_0}, \tag{7}$$

where $\Gamma(2-n)$ is the Euler gamma-function, $n < 2$, and $\kappa > 1$. The total amount of available rotational energy depends on the exact initial spin-down power and its time evolution. We use Eq. (2), which for $t \gg \tau_0$, gives $W_0 = \dot{E}_0\tau_0$, while for $t \sim \tau_0$, there is a correction factor of $(1+t/\tau_0)^{(\kappa+1)/(\kappa-1)}$.

We are agnostic on the exact values of η and n of each pulsar, but x-ray and γ-ray observations suggest values of $n \simeq 1.4$–2.0 [72–80], even though observations of gamma rays from the Crab pulsar reveal a significantly softer spectrum for the high-energy CR $e^{\pm}$ [74,78]. There are thus significant observed source-to-source variations among pulsars, especially at higher energies. In our simulations, we do not assume that all pulsars have the same values of CR $e^{\pm}$ injection indexes and spin-down power efficiencies (to CRs). Instead, the parameter n follows a uniform distribution $g(n)$. We use two different assumptions for $g(n)$ in assigning an injection index n to each pulsar of a given simulation; they are

$$n\epsilon\begin{cases}[1.6, 1.7], & \text{option "a"}\\ [1.4, 1.9], & \text{option "b".}\end{cases} \tag{8}$$

Similarly, each pulsar in a given simulation has a value of η taken from a log-normal distribution [20],

$$h(\eta) = \frac{\text{Exp}\left\{-\frac{[-\mu+\ln(-1+\eta)]^2}{2\sigma^2}\right\}}{\sqrt{2\pi}(\eta-1)\sigma}. \tag{9}$$

We do not know what the exact range of the η values should be. We therefore have in our simulations three options in choosing values for μ and σ in Eq. (9). The more physically intuitive quantities are the mean efficiency $\bar{\eta} = 1 + \text{Exp}\{\mu + \frac{\sigma^2}{2}\}$ and the parameter $\zeta = 10^{\sqrt{\sigma}}$. For a given produced simulation, ζ is fixed but $\bar{\eta}$ is normalized to the CR data. The three choices for log-normal distributions $h(\eta)$ are

$$(\bar{\eta},\zeta) = \begin{cases}(2\times10^{-2}, 1.29), & \text{option "a"}\\ (4\times10^{-3}, 1.47), & \text{option "b"}\\ (1\times10^{-3}, 2.85), & \text{option "c",}\end{cases} \tag{10}$$

TABLE I. The parameters for each of our five ISM propagation models; see Eqs. (11) and (12) and text for details.

Model	b ($\times 10^{-6}$ GeV^{-1} kyr^{-1})	D_0 (pc^2/kyr)	δ
A1	5.05	123.4	0.33
C1	5.05	92.1	0.40
C2	8.02	92.1	0.40
C3	2.97	92.1	0.40
E1	5.05	58.9	0.50

where the $\bar{\eta}$ values refer to the starting point before the fit. Typically, the values of $\bar{\eta}$ do not change by more than a factor of a few, with large values of ζ leading to smaller values of $\bar{\eta}$.

We note that the pulsars population does in fact have a distribution on the injection upper cutoff $E_{\rm cut}$. Yet, given that we have already observed TeV energy gamma rays from some of these sources (Geminga and Monogem) [6], we expect that these upper cutoffs will lay in the TeV range. For these values of cutoffs, the exact assumptions on $E_{\rm cut}$ do not affect our results, as $e^{\pm}$ that propagate into the ISM cool down very rapidly. In this work we take $E_{\rm cut} = 10$ TeV. For an electron starting at the cutoff energy of 10 TeV and under ISM model C1 of Table I, the typical time-scale for it to lose its energy down to 100 GeV is $\simeq$2 Myr. If instead we had taken the initial energy $E_{\rm cut}$ to be 1(100) TeV then the cooling down to 100 GeV time-scale would be different by only 10(1)%.

4. Propagation of cosmic rays

Cosmic rays injected into the ISM by individual pulsars have to travel from their simulated locations in the Milky Way to the Earth's location where they are detected by the *AMS-02*, *DAMPE*, and *CALET* instruments. They propagate first through the ISM before entering the volume affected by the solar magnetic field and wind. During that first propagation, the $e^{\pm}$ diffuse through the complicated galactic magnetic-field structure and lose energy via synchrotron radiation as well as ICS with the CMB and ambient infrared and optical photons. The first process is described by the diffusion coefficient,

$$D(E) = D_0 (E/1\ \text{GeV})^{\delta}, \tag{11}$$

assumed for simplicity to be homogeneous and isotropic within a thick several-kpc diffusion disc around the Milky Way stellar disc, where the pulsars reside. The energy losses are described by

$$dE/dt = -bE^2, \tag{12}$$

where b is proportional to the sum of the energy densities of the local (within a few kpc) magnetic field $U_{\rm B}$ and the local radiation field $U_{\rm rad}$. Relying on previous studies of the CR boron-to-carbon (B/C) ratio observed by both *PAMELA* and *AMS-02* and also on the CR proton data observed by *PAMELA* and *Voyager 1*, [21,81,82] we adopt five different ISM models for the CR propagation in our analysis. These are described in Table I.

After their ISM propagation and before their detection, CRs travel through the time-evolving solar wind. For energies $E \leq 10$ GeV, the effect on the CR spectra is known as solar modulation. This is the imprint of the diffusion, drift, and adiabatic energy losses experienced by CRs traveling through the complex magnetic field structure of the heliosphere (within $\simeq$100 au from the Sun). This solar modulation is described by imposing a translation in the energy of the CR spectra as [83],

$$\frac{dN^{\oplus}}{dE_{\rm kin}}(E_{\rm kin}) = \frac{(E_{\rm kin}+m)^2 - m^2}{(E_{\rm kin}+m+|Z|e\Phi)^2 - m^2} \times \frac{dN^{\rm ISM}}{dE_{\rm kin}}(E_{\rm kin}+|Z|e\Phi). \tag{13}$$

Here, $E_{\rm kin}$ is the observed kinetic CR energy at Earth ($\oplus$), while $\frac{dN^{\oplus({\rm ISM})}}{dE_{\rm kin}}$ the differential CR flux at Earth. The equivalent $E_{\rm kin}$ for the ISM spectrum is (on average) $E_{\rm kin} + |Z|e\Phi$, where Φ is the modulation potential. Finally, $|Z|e$ is the absolute value of the CR charge.

Ref. [82] used archival data to obtain a time-, charge- and rigidity(R)-dependent formula

$$\Phi(R,q,t) = \phi_0 \left(\frac{|B_{\rm tot}(t)|}{4\ \text{nT}}\right) + \phi_1 H(-qA(t)) \left(\frac{|B_{\rm tot}(t)|}{4\ \text{nT}}\right) \times \left(\frac{1+(R/R_0)^2}{\beta(R/R_0)^3}\right) \left(\frac{\alpha(t)}{\pi/2}\right)^4 \tag{14}$$

for the solar modulation potential. Following that work, R_0 is set to 0.5 GV. Instead ϕ_0 and ϕ_1 are marginalized within [0.32, 0.38] GV and [0, 16] GV, respectively, as was shown in Ref. [82] to be the proper range of the relevant uncertainties and in agreement with cosmic-ray observations. The values for $B_{\rm tot}(t)$ and $\alpha(t)$ are averaged over 6-month periods using the measurement by the *ACE* satellite [84] and the models of the Wilcox Solar Observatory [85]. The potential $\Phi(R,q,t)$ is time dependent for every species, different between electrons and positrons observed at the same time and rigidity, and is smaller for larger rigidities becoming $\Phi(R,q,t) \to \phi_0 (|B_{\rm tot}(t)|)/(4\ \text{nT})$.

5. Combining all the pulsar-population uncertainties

To combine all the astrophysical uncertainties, we first generate a pulsar population in the Milky Way with an assumed spatial distribution and birth rate, and a given choice of κ, τ_0, and $f(y)$ characterizing the initial spin-down power and its evolution. There are 30 different combinations of these assumptions (see Appendix A of [20] for details). These pulsars also follow the distributions

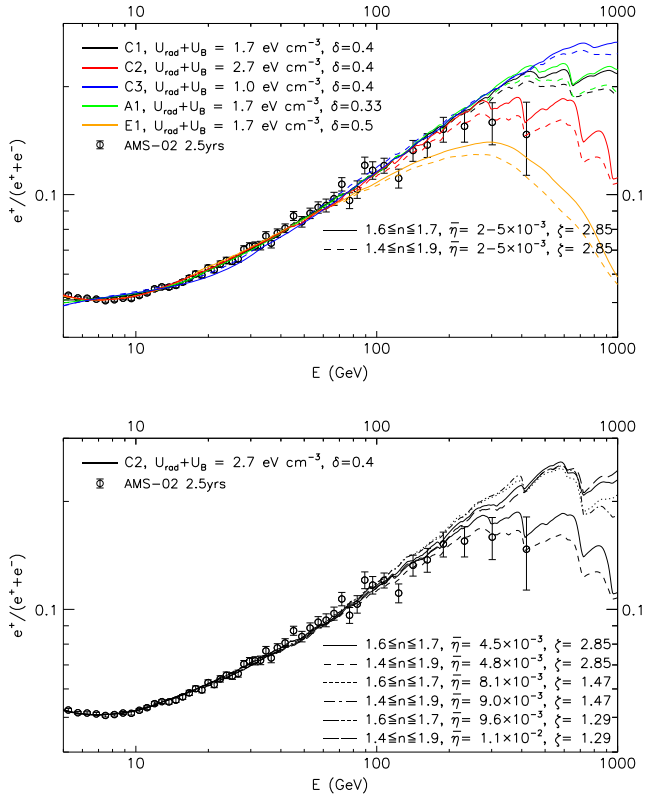

FIG. 3. The effects of changing assumptions in our astrophysical pulsars realizations. *Top:* Different color lines depict the effect that changing only the CR propagation through the ISM [i.e., CR diffusion and energy-losses described by Eqs. (11) and (12)] has on the expected flux from what is otherwise the same simulation of pulsar sources in the Milky Way. ISM Models "C1", "C2", "C3", "A1" and "E1" are described in Table I. As described in the main text, we fit the simulations to the *AMS-02* data. The solid vs dashed lines for every given colored line show the impact on our results of changing solely the distribution of the CR injection indexes $g(n)$ [see Eq. (8) and also Eq. (5)]. *Bottom:* For a specific assumption on the ISM propagation conditions ("C2"), we show in the six types of lines, the effect of varying the assumptions on $g(n)$ and $h(\eta)$ (see Eqs. (5) and (8)–(10), respectively, and discussion therein).

$g(n)$ and $h(\eta)$ on the injection properties. There are six combinations for these two distributions, which we refer to as "aa", "ba", "ab", "bb", "ac", and "bc", where the first letter refers to the $g(n)$ options "a" or "b" of Eq. (8) and the second letter to $h(\eta)$, with its options "a-c" of Eq. (10). We also choose one of the five ISM propagation models described by Table I, while we marginalize over parameters ϕ_0 and ϕ_1 of Eq. (14) to account for solar modulation. Those choices result in $30 \times 6 \times 5 = 900$ different astrophysical realizations/simulations that we test.

Each one of these astrophysical realizations is fitted to the CR data by allowing for five fitting parameters, ϕ_0, ϕ_1, the normalization of the primary CR electron flux, the normalization of the secondary CR $e^{\pm}$ fluxes and the normalization of the total pulsar CR $e^{\pm}$ fluxes at the location of the Sun (outside the heliosphere).[1] The impact of these different astrophysical choices on the positron fraction spectrum is given in Fig. 3. The five different colored lines refer to the five ISM models.

In the top panel of Fig. 3 and for the choice "c" of $h(\eta)$, we give the two choices for $g(n)$; i.e., the choices "ac" and "bc" in solid and dashed lines, respectively. Different ISM assumptions can enhance ("A1", "C2" choices) or suppress ("C3", "E1" choices) the small-scale (in energy range) features of the spectra. At high energies when the energy-loss rate is assumed to be larger (smaller) or the CR diffusion slower (faster), the small-scale spectral features are more (less) pronounced. Similarly, when a wider range of injection indexes n is assumed, the resulting features are more evident (from the fact that Poisson fluctuations of nearby sources with hard injected spectra being dominant are more common). Moreover, since the fits are dominated by the low-energy data, different ISM models can predict significant variations at high energies. For instance, "A1" models faster diffusion of low-energy CRs, but with a smaller diffusion index $\delta = 0.33$, which in turn increases the escape timescale of CRs from the Galaxy, and thus enhancing their flux at high energies. Model "E1" represents the reverse assumption (slow diffusion of low-energy CRs but with a larger diffusion index $\delta = 0.5$ leading to faster escape at high energies) suppressing the high-energy fluxes. Model "C1" represents a more intermediate case. Also, larger/smaller energy losses (modeled by "C2"/"C3") suppress/enhance the high-energy CR pulsar fluxes.

The bottom panel of Fig. 3 shows, for a fixed choice ("C2") of ISM assumptions, the impact of varying the $g(n)$ and $h(\eta)$ choices. A wider range of the ζ parameter, associated with the standard deviation in the $h(\eta)$, results in more pronounced features. We also note that when ζ is larger, a few pulsars may deposit a larger fraction of their spin-down power to CR $e^{\pm}$ in the ISM. In turn, the fits are forced to compensate for that by reducing the averaged $\bar{\eta}$ value.

III. RESULTS

A. Using only the *AMS-02* positron fraction data

Our fits to the *AMS-02* positron-fraction spectrum allow us to constrain combinations of the above mentioned astrophysical uncertainties via data not previously used to probe the pulsar population properties of the Milky Way. Of the 900 astrophysical realizations, only 205(160) can fit the positron fraction spectrum within $3\sigma(2\sigma)$ from an

[1]The ranges of ϕ_0 and ϕ_1 are described in Sec. II B 4, while the normalization of the primary CR electron and the secondary CR electron and positron fluxes are such that at low energies the pulsars component is highly subdominant as expected. For instance, at 10 GeV, pulsars contribute only $\simeq$20% of the positron fraction and $\simeq$1% of the total $e^+ + e^-$ flux; while at 5 GeV their contribution is only $\simeq$5% to the positron fraction and $O(0.1)$% to the total flux.

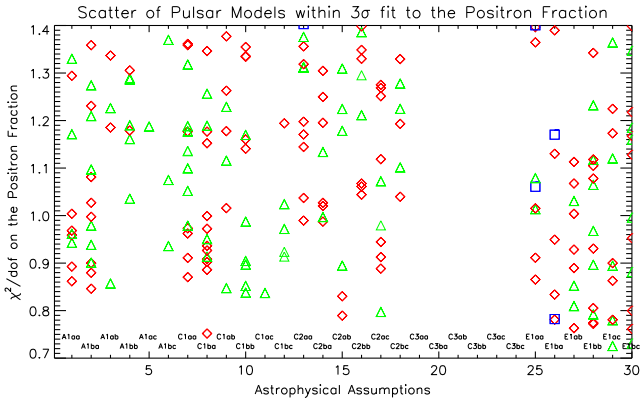

FIG. 4. The scatter of astrophysical pulsar realizations that fall within our 3σ constraint to the *AMS-02* positron fraction data. On the y-axis we give the χ^2/d.o.f. value, while on the x-axis we give the astrophysical assumptions, e.g., "A1aa" refers to ISM model "A1" and $g(n)$ and $h(\eta)$ distributions choice "aa" of Eqs. (8) and (10), respectively. Blue boxes are for braking index κ of 2.5, red diamonds for $\kappa = 3.0$ and green triangles for $\kappa = 3.5$. Two evident results are that i) very few pulsar population realizations with $\kappa = 2.5$ survive the positron fraction fit and ii) there are no realizations with ISM conditions "C3" allowed by the data (see text for further details).

expectation of χ^2 of 1 for each degree of freedom (d.o.f.)[2] These astrophysical realizations are depicted in Fig. 4.

In Fig. 4, the y-axis gives the χ^2 per d.o.f. for the positron fraction data. The x-axis represents the probed parameter space in 30 distinct combinations of assumptions. These mark the assumptions on the CR $e^{\pm}$ ISM propagation described by the first two characters ("A1", "C1", "C2", "C3", "E1") as well as the CR injection properties both with regards to the injection index n-distribution $g(n)$ of Eq. (8) and the $h(\eta)$ distribution of Eq. (10). The latter assumptions are depicted by the last two characters ("aa", "ba", "ab", "bb", "ac", "bc"). For example the first discrete point in the x-axis ("A1aa") refers to ISM model "A1" of Table I while the third character "a" stands for $n\epsilon[1.6, 1.7]$ and the last character for $(\bar{\eta}, \zeta) = (2 \times 10^{-2}, 1.29)$ (case "a"). Each allowed pulsar population simulation is represented by a shape. Blue boxes are for $\kappa = 2.5$, red diamonds are for $\kappa = 3.0$ and green triangles for $\kappa = 3.5$.

From our fits to the positron fraction, we have two major findings. The first is that while we run 240 realizations with a braking index of $\kappa = 2.5$, only 5(3) survive within the 3(2) σ fit threshold. While there are constraints from radio observations on the period and NS surface B-field, we try to adopt as wide as possible assumptions on the initial spin-down properties of the pulsar populations. These wide assumptions have a significant impact also on the observed pulsar populations as we show in Fig. 2. For the braking index value of 2.5 assumed in the 240 simulations, values for τ_0 are in the range of 0.6–1 kyr and of $10^{x_{\rm cutoff}}$ from $10^{38.2}$–10^{39} erg/s with varying assumptions on μ_y and σ_y (see Eqs. (2) and (4) and Appendix B of [20]). Our second major finding relates to the ISM conditions. For every choice of NS population birth distribution, spin-down properties and pulsars injection of CR $e^{\pm}$ properties, we test each of our five ISM models. Our model "C3" is always excluded as can be seen by the gap in the parameter space in Fig. 4. Table II describes the above and provides the fraction of simulations that are allowed by the data (at 3σ) with the exact number of simulations given in the parentheses.

TABLE II. For combinations of the three choices of braking index $\kappa = 2.5$, 3.0, 3.5 and the five choices of ISM propagation conditions "A1", "C1", "C2", "C3", "E1", we give the fraction of pulsar population simulations that are consistent (within our 3σ threshold) to the *AMS-02* positron fraction spectrum. In the parentheses we give the actual number of the simulations allowed. For the combination of $\kappa = 3$ and "A1" we produced 78 simulations to probe the remaining astrophysical parameters, of which 21 (27%) are allowed.

	A1	C1	C2	C3	E1
$\kappa = 2.5$	0 (0)	0 (0)	0.02 (1)	0 (0)	0.08 (4)
$\kappa = 3.0$	0.27 (21)	0.40 (31)	0.40 (31)	0 (0)	0.46 (36)
$\kappa = 3.5$	0.37 (20)	0.43 (23)	0.35 (19)	0 (0)	0.41 (23)

Both sets of assumptions (i.e., $\kappa = 2.5$ or ISM model "C3") systematically predict a higher positron fraction than observed above 100 GeV. For the case of the ISM "C3" model, this is straightforward given the suppressed energy-loss coefficient b of Eq. (12). For $\kappa = 2.5$, the explanation is as follows. Smaller braking index values demand not only a smaller characteristic timescale τ_0, but also result in a faster spinning-down of the pulsars at $t \gg \tau_0$, e.g., $\dot{E}(t) \propto t^{-2.33}$ for $\kappa = 2.5$ vs $\dot{E}(t) \propto t^{-2}$ for $\kappa = 3$ [see Eq. (2)]. In setting the spin-down choices of our pulsar population simulations, we rely on radio observations. These observations probe a wide range of pulsar ages, but there are many more pulsars of age 1–10 Myr than of 10–100 kyr. In our simulations, we check that our pulsar populations are consistent with the late-age properties of the observed pulsars and then effectively evolve backwards in time the pulsars spin-down. Yet, as we explained in Sec. II, most of the pulsars CR flux is produced in the early stages of their evolution. A more abrupt spin-down-power time-evolution as in the $\dot{E}(t) \propto t^{-2.33}$ vs $\propto t^{-2}$ case predicts a higher CR flux overall from each pulsar at a level that is already inconsistent with the CR *AMS-02* data. Values of $\kappa < 2.5$, as are observed for some of the youngest pulsars, are excluded. Hence, CR data also suggest a time evolution of the braking index.

[2]There are 51 energy bins for the positron fraction in the energy range of 5 to 500 GeV that we fit. Since in the fitting, we have five free parameters (as discussed in Sec. II), there are 46 d.o.f. leading to a total χ^2 of 64.2 and 57.3, respectively, for the quoted 3σ and 2σ ranges assuming as a starting point a χ^2/d.o.f. = 1.

TABLE III. As in Table II, we present, for the combination of the six choices ("aa", "ba", "ab", "bb", "ac" and "bc") of $g(n)$ and $h(\eta)$ and the five ISM models, the fraction of pulsar simulations that are consistent within 3σ with the *AMS-02* positron fraction. The numbers in parentheses give the number of the simulations allowed.

		A1	C1	C2	C3	E1
aa	$1.6 \leq n \leq 1.7$, $\eta = 2 \times 10^{-2}$, $\zeta = 1.29$	0.37 (11)	0.43 (13)	0.36 (11)	0 (0)	0.33 (10)
ba	$1.4 \leq n \leq 1.9$, $\eta = 2 \times 10^{-2}$, $\zeta = 1.29$	0.46 (14)	0.50 (15)	0.27 (8)	0 (0)	0.23 (7)
ab	$1.6 \leq n \leq 1.7$, $\eta = 4 \times 10^{-3}$, $\zeta = 1.47$	0.13 (4)	0.23 (7)	0.27 (8)	0 (0)	0.33 (10)
bb	$1.4 \leq n \leq 1.9$, $\eta = 4 \times 10^{-3}$, $\zeta = 1.47$	0.23 (7)	0.36 (11)	0.33 (10)	0 (0)	0.43 (13)
ac	$1.6 \leq n \leq 1.7$, $\eta = 1 \times 10^{-3}$, $\zeta = 2.85$	0.07 (2)	0.07 (2)	0.27 (8)	0 (0)	0.33 (10)
bc	$1.4 \leq n \leq 1.9$, $\eta = 1 \times 10^{-3}$, $\zeta = 2.85$	0.10 (3)	0.17 (5)	0.20 (6)	0 (0)	0.43 (13)

TABLE IV. Similar to the slices in parameter space given in Tables II and III, we show for the combination of the six choices of $g(n)$ and $h(\eta)$ and the three choices for braking index $\kappa = 2.5$, 3.0, 3.5, the fraction of pulsar population simulations that are consistent within 3σ with the *AMS-02* positron-fraction spectrum. As before, in the parentheses the actual number of our simulations allowed are given.

		$\kappa = 2.5$	$\kappa = 3.0$	$\kappa = 3.5$
aa	$1.6 \leq n \leq 1.7$, $\eta = 2 \times 10^{-2}$, $\zeta = 1.29$	0.08 (3)	0.38 (25)	0.36 (16)
ba	$1.4 \leq n \leq 1.9$, $\eta = 2 \times 10^{-2}$, $\zeta = 1.29$	0.05 (2)	0.48 (31)	0.27 (12)
ab	$1.6 \leq n \leq 1.7$, $\eta = 4 \times 10^{-3}$, $\zeta = 1.47$	0 (0)	0.26 (17)	0.27 (12)
bb	$1.4 \leq n \leq 1.9$, $\eta = 4 \times 10^{-3}$, $\zeta = 1.47$	0 (0)	0.32 (21)	0.44 (20)
ac	$1.6 \leq n \leq 1.7$, $\eta = 1 \times 10^{-3}$, $\zeta = 2.85$	0 (0)	0.15 (10)	0.22 (10)
bc	$1.4 \leq n \leq 1.9$, $\eta = 1 \times 10^{-3}$, $\zeta = 2.85$	0 (0)	0.17 (11)	0.33 (15)

Moreover, we note that changing the braking index to $\kappa \geq 3$ is enough to exclude the tension with the positron fraction data. Yet as more events are detected from *AMS-02* and if indeed a cutoff/dropoff the positron fraction above 500 GeV is confirmed, we will be able to probe/exclude more simulations with $\kappa = 3$. The ISM model "A1" that predicts higher CR fluxes due to its diffusion parameters (see Table I and Fig. 3 *top*) is currently only mildly less preferred as shown also in Table II, but we do find that with an observed dropoff of the positron fraction above 500 GeV, many pulsar simulations with the "A1" assumptions can be excluded, while ISM model assumptions "E1" will be slightly preferred ("C1" and "C2" being less affected by the presence of the claimed cutoff).

In addition to the above findings, we note a preference among astrophysical realizations that predict a narrower distribution $h(\eta)$, in the fraction of the spin-down power that goes into CR $e^{\pm}$, with ζ following hierarchically option "a" ($\zeta \equiv 10^{\sqrt{\sigma}} = 1.29$) over option "b" ($\zeta = 1.47$) over option "c" ($\zeta = 2.85$) as described by Eqs. (9) and (10). This can be seen more directly by our results in Table III, where we show the slice in parameter space describing the combination of $g(n)$ and $h(\eta)$ injection properties vs the five ISM propagation models. For the narrower $h(\eta)$, anywhere between 23% and 50% of our simulations are within our threshold of fit to the positron fraction data. For the wider distribution choices, these fractions are reduced with the widest choice (choices "ac" and "bc") having anywhere between 7% to 43% of the simulations within our 3σ fitting threshold.

We have found no preference towards a narrower or a wider distribution for $\dot{E}_0$—i.e., for the parameter σ_y of Eq. (4).

While still more data from CRs will be necessary, the preference towards a narrow $h(\eta)$ suggests that the pulsar environments do not have very wide source-to-source variations with respect to their output of CR $e^{\pm}$ injected into the ISM.

Finally, we find that there is only a slight preference for the wider $g(n)$ injection index n-distribution (option "b" of Eq. (8) over the narrower one (option "a" of Eq. (8). This is evident in the slice of parameter space in Table IV showing the $g(n)$, $h(\eta)$ parameters versus the braking index κ.

We note that more data are being collected by the *AMS-02* experiment that can confirm these first indications of preferences in the parameter space of pulsar population properties. In particular, we expect that if a clear cutoff in the positron fraction is observed above 500 GeV in energy, then a significant fraction of the 205 pulsar astrophysical realizations will be excluded.

B. Including data from *CALET* or *DAMPE*

Recently, two more satellite experiments, *CALET* [27] and *DAMPE* [25], have published their measurements of the total $e^+ + e^-$ CR flux up to 5 TeV [26,29]. These spectra allow us to test pulsar-population models at energies where their expected fractional contribution to the total measured quantities can be very significant. For instance at 50 GeV, our fits suggest that the pulsar population is responsible for

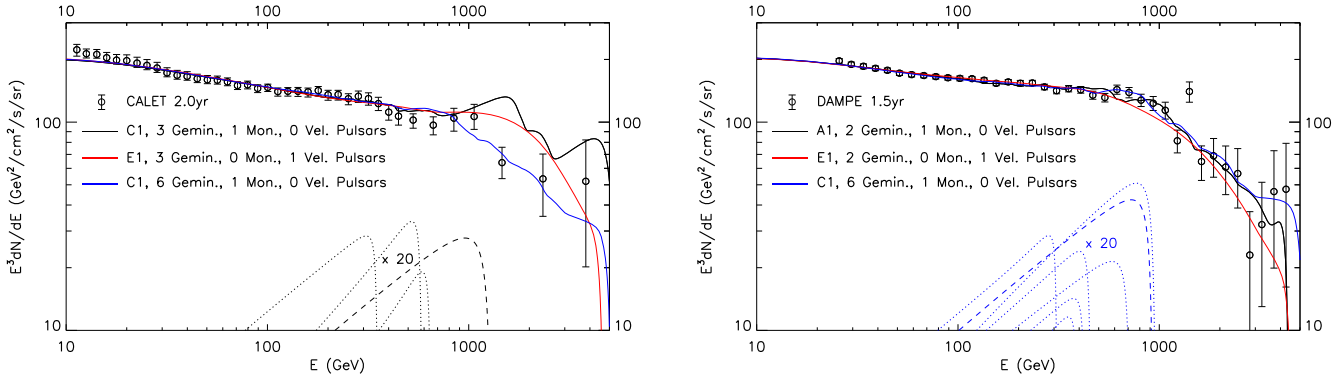

FIG. 5. The simulated $e^+ + e^-$ fluxes from combinations of pulsars. We include the primary e^- and secondary $e^\pm$ CR components. On the *left* panel we present three simulations that fit well the *CALET* spectral data depicted, while in the *right* panel we do the same with the *DAMPE* spectral data. For the simulations presented we give the number of pulsars that have age, distance from Earth, and current spin-down power in agreement with the observed ones of Geminga ("Gemin"), Monogem ("Mon") and Vela ("Vel") (see text for details). At high energies, we note the presence of several features coming from the contribution of individual pulsars and also a cutoff/change of slope to the total $e^\pm$ flux above a TeV due to a small number of contributing sources. We also present for one simulation the fluxes from the individual pulsars that have properties similar to those of Geminga (dotted lines) and Monogem (dashed lines). These fluxes are multiplied by a factor of 20 to lie within the panels' range. There are large source-to-source variations in our simulations even among Geminga-like pulsars, as we describe in the text.

≃50% of the measured positron fraction value but only for ≃8% of the observed $e^+ + e^-$ flux. At 500 GeV, pulsars can instead be responsible for as much as 90% of the positron fraction and up to 40% of the $e^+ + e^-$ flux, with the pulsar contribution becoming potentially even more important at higher energies.

1. The highest energies: understanding the young, nearby pulsars

At higher energies, the combination of volume and age necessary for pulsars to be able to contribute is reduced. Thus the number of sources drops, with the highest energies probing only a small number of pulsars. This should result in $e^+ + e^-$ fluxes rich in features as is shown in Fig. 5, where we compare some of our simulations to the data from *CALET* (left) and *DAMPE* (right). Additionally at ≃1 TeV, we find in our simulations that even after smoothing the possible small-scale features, there is typically either a cutoff in the $e^+ + e^-$ flux spectrum or a change in its slope. This is attributed to the fact that only $O(10)$ pulsars can contribute at these energies. The exact energy that this change in the spectrum occurs at and the resulting spectral characteristics depend on these pulsars' individual properties.

In order to understand the impact of some known nearby pulsars, we compare with similar pulsars in our simulations that fall in our neighborhood. There is extended literature on the possible contribution from Geminga (J0633 + 1746) and Monogem (B0656 + 14) to the high-energy positron flux [6,8,86–92]. We test the possible contribution from these pulsars by identifying simulations that have pulsars with the same combination of distance from the Earth, age, and current spin-down luminosity as these two pulsars. More specifically, we check for pulsars with (distance, age, $\dot{E}(t = \text{age})$) that are within the (distance central value $\pm 1\sigma$, spin-down age$^{+100\%}_{-50\%}$, spin-down luminosity$^{+100\%}_{-50\%}$) of the reported ($0.25^{+0.45}_{-0.09}$ kpc, 3.42×10^5 yr, 3.2×10^{34} erg/s) for Geminga and (0.29 ± 0.15 kpc, 1.11×10^5 yr, 3.8×10^{34} erg/s) for Monogem [47,48]. We note that the spin-down age and luminosity rely on the measurements of the period P and its time derivative $\dot{P}$ and are calculated assuming a braking index of $\kappa = 3$. Since we want to be agnostic about the true braking index, we allow for the wide range around the central values of age and luminosity. Furthermore, we check for simulations with pulsars that have similar properties as Vela (B0833 − 45) (0.28 ± 0.14 kpc, 1.13×10^4 yr, 6.9×10^{36} erg/s).

In both panels of Fig. 5 we show the CR spectra from three simulations that can explain the data. For each of these simulations the number of pulsars that have distance, age, and luminosity properties similar to Geminga, Monogem, and Vela are provided. It is typically easier to get pulsars like Geminga and Monogem, while a pulsar like Vela is relatively rare. Out of our simulations that fit the positron-fraction data, 75% have at least one Geminga-like and 18% at least one Monogem-like pulsar, while only 3% have at least one Vela-like pulsar. We note that in many of our simulations Geminga-like and Monogem-like pulsars contribute O(1)% of the total $e^+ + e^-$ flux at energies close to their relevant cooling cutoffs (see Fig. 5).

In each of the Fig. 5 panels, for a chosen simulation, we also plot the predicted $e^+ + e^-$ fluxes from these particular pulsars. Since Vela-like pulsars are younger, their contribution can be dominant only above a few TeV, but the suppression of the total flux suggests that Vela is not a dominant source of $e^\pm$ either because these CRs have

not yet reached us or because its η is suppressed. In fact recent work from Ref. [93] suggests that a significant fraction of high energy CRs from very young pulsars (as is Vela) are strongly confined for $O(10)$ kyr before being released into the ISM. Monogem-like pulsars contribute at $\simeq$1 TeV energies and Geminga-like pulsars at $\simeq$500 GeV. The exact cutoff energy depends on the ISM energy-losses rate and the individual pulsar's age. Even after fixing the ISM model and comparing only among the Geminga-like pulsars, there are source-to-source variations in the cutoff due to the age uncertainty that we include for these sources. The amplitude instead depends on their distance from Earth (that in turn has variations since we allow an uncertainty on this as well) and also on the η parameter that is unique to each source. Finally the slope for energies lower than the cutoff depends on the diffusion assumptions and on the individual/unique pulsar injection index n (for further details see Ref. [21]).

We note, that we do not over-plot the *CALET* and *DAMPE* spectral data and we do not try to fit our simulations simultaneously to both. The measured spectral indexes of the $e^+ + e^-$ flux are in some disagreement between these data-sets, suggesting some energy-scale-related measurement uncertainty.

2. Combining AMS-02 and CALET data

Instead, we combine the *AMS-02* separately with the *CALET* data. We do that by taking all the original 900 simulations with their best χ^2 fit free-parameter values to the positron fraction and test their predicted $e^+ + e^-$ flux to the measurements by *CALET* and *DAMPE,* respectively. We have noticed that, as is also discussed in Ref. [29], the *CALET* fluxes agree pretty well with the *AMS-02* data.[3] For each simulation, in fitting to the *CALET* (*DAMPE*) $e^+ + e^-$ data, we allow for an additional 10(20)% freedom in the primary e^-, secondary $e^\pm$ and pulsars $e^\pm$ normalizations starting from the best fit values to the positron fraction.[4] Since all the data points are above 10 GeV in energy, the impact of solar modulation is insignificant, and we do not refit the relevant ϕ_0, ϕ_1 parameters.

In Fig. 6 (top panel), we give the scatter of pulsar realizations that are in agreement with the *AMS-02* and *CALET* data within 3σ from what is a χ^2/d.o.f. of 1.[5] The axes are the same as in Fig. 4 with the exception that the y-axis now refers to the combined data fit. As in Sec. III A, we portray the three tested values for the braking index κ with there different symbols (boxes, diamonds and triangles for the simulations with $\kappa = 2.5$, 3.0 and 3.5). Comparing to the $e^+ + e^-$ flux data, it is easy to acquire a

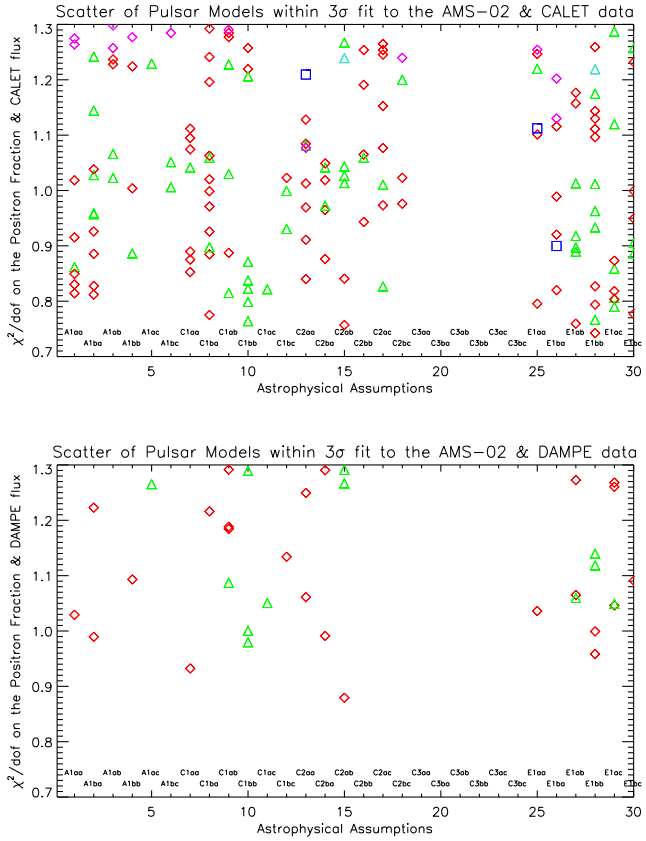

FIG. 6. As in Fig. 4, we present the scatter of astrophysical pulsar realizations that fall within our 3σ constraint to the combined *AMS-02* positron fraction and *CALET* (*top* panel) or *DAMPE* (*bottom* panel) $e^+ + e^-$ flux data. The y-axis is the χ^2/d.o.f. value for the combined data (see text for details), while the x-axis describes the same astrophysical assumptions as in Fig. 4. For each of the three values of braking index that we test, we depict realizations by two colors depending on the quality of their fit to the positron fraction alone. For braking index κ of 3.0, the red diamonds are for simulations allowed within 3σ by the positron-fraction data. These same simulations are among the 205 simulations described in Sec. III A. With magenta diamonds we depict models allowed within 3σ by the combined data, but that are excluded by *AMS-02* data alone. Similarly, for $\kappa = 3.5$, green (turquoise) triangles show the realizations allowed (excluded) by the *AMS-02* positron fraction. No additional models with $\kappa = 2.5$ are allowed by adding the *CALET* measurement. With *DAMPE* data there are no blue, magenta and turquoise symbols.

[3]We also tested the earlier results by the *CALET* collaboration published in [28]. These data also agree well with the *AMS-02* measurements.

[4]In theory we could have fitted the three normalizations simultaneously to the *AMS-02 & CALET* or *AMS-02 & DAMPE* spectra. We choose that approach instead, since from the comparison of *CALET* and *DAMPE*, we understand that energy-scale systematic errors between different experiments can be important. We also allow for greater freedom when combining with the *DAMPE* data to reduce the possible impact of these systematics. The 20% is also close to the upper limit of some of these parameters uncertainties.

[5]There are 51 *AMS-02* data points fitted by 5 d.o.f. and 39 *CALET* or *DAMPE* data points fitted by 3 additional parameters. For the remaining 82 d.o.f. for 3σ, the combined χ^2/d.o.f $= 1.288$.

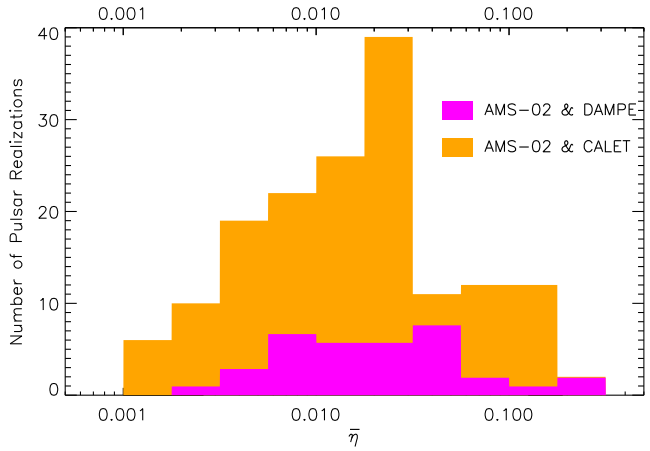

FIG. 7. The distribution of the fitted values of the $\bar{\eta}$ parameter for the pulsar-population simulations, allowed within 3σ by the combination of *AMS-02 & CALET* data (159 astrophysical pulsar realizations in the orange histogram), or allowed by the *AMS-02 & DAMPE* data (36 in the magenta histogram).

good fit. In fact, of the 205 simulations that are allowed within the 3σ threshold by the positron fraction data, 145 are also allowed by the combined positron fraction and $e^+ + e^-$ flux data. As in Fig. 4, those are shown by the blue boxes, red diamonds, and green triangles, respectively. Some pulsar astrophysical realizations have a good enough fit to the *CALET* data and although not allowed within the 3σ threshold by only *AMS-02*, are allowed by the combined data. There are 14 such simulations in addition to the 145. We show these by magenta diamonds and turquoise triangles for $\kappa = 3.0$ and 3.5, respectively, which typically lie on the top end of the y-axis. No additional models with $\kappa = 2.5$ were added in the analysis by including the *CALET* data.

We find that, as with the positron fraction fit, ISM model "C3" is systematically excluded by the data regardless of the other astrophysical assumptions. In fact, the addition of the flux data does not alter the conclusions of Sec. III A or set further preferences among the remaining ISM models. Similarly, it is still the case that only a small number of simulations with $\kappa = 2.5$ (3 out of 159) are allowed, and beyond that, adding the flux data only slightly affects the preference for simulations with $\kappa = 3.0$ versus 3.5. Regarding the fraction of the spin-down power going into CR $e^{\pm}$, the preference for narrower $h(\eta)$ is sustained, while the $g(n)$ index of injection distribution properties conclusions are unaffected by the *CALET* data.

In Fig. 7, we also present a histogram of the fitted values of the mean fraction $\bar{\eta}$ of the pulsars population from each realization. The number on the y-axis is the number of these pulsar astrophysical realizations that are allowed. The range of $\bar{\eta}$ to explain the CR data is between 10^{-3} and 0.26, with a clear peak at $1\text{–}3 \times 10^{-2}$. These fractions assume a Milky Way pulsar birth rate of one per century. If that rate is doubled, those fractions are smaller by the same factor.

3. Combining AMS-02 and DAMPE data

On the other hand, combining the *DAMPE* $e^+ + e^-$ flux data with the *AMS-02* positron fraction dramatically cuts down the parameter space of the pulsar astrophysical realizations allowed (see bottom panel of Fig. 6). Out of the 205 simulations allowed by the positron-fraction data, only 36 remain after combining with *DAMPE*, while the down-weighting of the *AMS-02* data does not lead to any additional simulations allowed within the 3σ threshold. We find that none of the $\kappa = 2.5$ simulations survive, while 2/3 of these astrophysical realizations are with $\kappa = 3$. Regarding the impact of these data on the ISM and $h(\eta)$, $g(n)$ distributions: our results discussed above hold given the small number of remaining simulations. The range of $\bar{\eta}$ is basically the same as that from *CALET* and *AMS-02* data (Fig. 7).

We finally note that tracking the source of the systematic difference between *CALET* and *DAMPE* $e^+ + e^-$ data is of great importance in properly combining the data in future analyses.

IV. DISCUSSION AND CONCLUSIONS

We have used CR $e^{\pm}$ data to study the properties of the population of local Milky Way pulsars. Using the *AMS-02* positron-fraction measurement and the *CALET* and *DAMPE* $e^+ + e^-$ fluxes, we have tested hundreds of pulsar simulations. These simulations probe the astrophysical uncertainties associated with the CR leptonic spectra observed at Earth. In particular, we produce 900 simulations that sample a broad range of possibilities for the spatial distribution of neutron-star birth locations in the Milky Way, for their ages, and their spin-down properties. We also study the effects of uncertainties in the spectra of CR $e^{\pm}$ injected into the ISM and those associated with CR propagation through the ISM. We describe how we model all these astrophysical effects and how we combine them in Sec. II.

We work under the assumption that pulsars are the dominant source for the rise of the positron fraction at high energies. We find that consistent pulsar-population models can result in a continued rise in the positron fraction with energy, a flattening at energies beyond 300 GeV, or even a dropoff. We also find that consistent models can produce a positron-fraction spectrum that is either smooth in energy or that has fluctuations with energy (see Fig. 1).

We find ISM models with energy losses that are suppressed relative to what is conventionally assumed [10,12,14], but that are still allowed within reasonable uncertainties on the local magnetic and interstellar-radiation fields, are excluded by either the *AMS-02* positron fraction data alone, or in combination with *CALET* or *DAMPE* data. The underlying reason for this result is that low energy losses cause the pulsar spectra (even after performing a χ^2 fit) to overshoot the current spectral data at high energies (where the energy losses have a dominant impact). Simulations probing other typical ranges of ISM

conditions are also performed as described in Sec. II, with the relevant results in Sec. III.

Furthermore, a pulsar braking index κ of 2.5 or less is disfavored by the data, regardless of most of the other astrophysical assumptions, with a very small fraction of our simulations with $\kappa = 2.5$ being allowed. In this work we consider pulsars to have a constant braking index throughout their time evolution, and set their population spin-down properties so that we can explain the radio-frequency observations from many such sources. These radio-pulsars are typically a Myr old. A braking index of 2.5 produces pulsars that are very powerful sources at their younger stages, when most of the CR $e^{\pm}$ are produced. Consequently, high energy data that probes younger pulsar sources is overshot by these simulations. We also find some small preference for a braking index of 3 versus 3.5, from the CR data. These results are also given in Figs. 4 and 6 and Tables II and IV.

Given that we have observed several very young pulsars (with ages of $O(10^4)$ yrs or less) with a braking index of less than 3, these results create a tension. One solution to that, would be that pulsars have time-variable braking indexes. For instance, pulsars might start with smaller indexes leading to fast spin-down in their initial stages. As the braking index increases to a value of $\simeq 3$, relevant for magnetic-dipole radiation, the pulsars spin down more slowly. If the braking index indeed changes with time, we will need additional simulations to probe all the possible paths of $\kappa(t)$, versus the $\kappa =$ constant studied in this work.

Since pulsars are observed to have large variations in their surface magnetic fields and original periods, we study the resulting distribution of their initial spin-down power as a population. We find no indications for any preference in terms of a narrow or a wide initial spin-down power distribution. Also, the fraction of rotational energy going to CR $e^{\pm}$ is very uncertain. By modeling it with a log-normal distribution, we find that the CR data fits hint at a narrow distribution for this fraction (see Figs. 4 and 6 and Tables III and IV). In terms of the averaged (of the pulsar-population) value, the fraction is fitted in half of our simulations to be $\simeq$1–3% (see Fig. 7). The exact injection spectral properties of pulsars are still not well constrained by the CR data.

The CR spectra above $\simeq$500 GeV, accessible currently by *CALET* and *DAMPE*, allow us to study young nearby pulsars. We find that above a TeV in energy, pulsar simulations can explain the observed change in the $e^+ + e^-$ slope, since the number of contributing sources drops to only $O(10)$. However, as this is a small number of pulsars, large variations in the predicted CR spectra are seen between simulations, associated with the properties of the individual contributing pulsars. Finally, the $e^{\pm}$ fluxes that are from young, nearby, and energetic pulsars (like Vela) are constrained by the data.

ACKNOWLEDGMENTS

We thank Joseph Gelfand, Victoria Kaspi, Ely Kovetz, Tim Linden, Dmitry Malyshev and Robert Schaefer for valuable discussions. This research project was conducted using computational resources at the Maryland Advanced Research Computing Center (MARCC) and supported by NASA Grant No. NNX17AK38G, NSF Grant No. 0244990, and the Simons Foundation.

[1] L. Kuiper, W. Hermsen, G. Cusumano, R. Diehl, V. Schonfelder, A. Strong, K. Bennett, and M. McConnell, The crab pulsar in the 0.75–30 MeV range as seen by cgro comptel, Astron. Astrophys. **378**, 918 (2001).

[2] L. Kuiper, W. Hermsen, and B. Stappers, Chandra and RXTE studies of the x-ray/gamma-ray millisecond pulsar PSR J0218 + 4232, in *34th COSPAR Scientific Assembly: The 2nd World Space Congress Houston, Texas, 2002* [Adv. Space Res. 33, 507 (2004)].

[3] D. J. Thompson, Gamma ray pulsars: Multiwavelength observations, Astrophysics and Space Science Library **304**, 149 (2004).

[4] B. M. Gaensler and P. O. Slane, The evolution and structure of pulsar wind nebulae, Annu. Rev. Astron. Astrophys. **44**, 17 (2006).

[5] A. U. Abeysekara *et al.*, The 2HWC HAWC observatory gamma-ray catalog, Astrophys. J. **843**, 40 (2017).

[6] A. U. Abeysekara *et al.* (HAWC), Extended gamma-ray sources around pulsars constrain the origin of the positron flux at Earth, Science **358**, 911 (2017).

[7] A. A. Abdo *et al.*, Milagro observations of TeV emission from Galactic sources in the Fermi bright source list, Astrophys. J. **700**, L127 (2009); Erratum, Astrophys. J. **703**, L185(E) (2009).

[8] D. Hooper, I. Cholis, T. Linden, and K. Fang, HAWC observations strongly favor pulsar interpretations of the cosmic-ray positron excess, Phys. Rev. D **96**, 103013 (2017).

[9] T. Linden, K. Auchettl, J. Bramante, I. Cholis, K. Fang, D. Hooper, T. Karwal, and S. W. Li, Using HAWC to discover invisible pulsars, Phys. Rev. D **96**, 103016 (2017).

[10] I. V. Moskalenko, A. W. Strong, J. F. Ormes, and M. S. Potgieter, Secondary anti-protons and propagation of cosmic rays in the galaxy and heliosphere, Astrophys. J. **565**, 280 (2002).

[11] M. Kachelriess, I. V. Moskalenko, and S. S. Ostapchenko, New calculation of antiproton production by cosmic ray protons and nuclei, Astrophys. J. **803**, 54 (2015).
[12] GALPROP code Website, http://galprop.stanford.edu/.
[13] E. Carmelo, D. Gaggero, D. Grasso, and L. Maccione, Cosmic-ray nuclei, antiprotons and gamma-rays in the galaxy: A new diffusion model, J. Cosmol. Astropart. Phys. 10 (2008) 018.
[14] DRAGON code website, http://dragon.hepforge.org.
[15] P. M. Dragicevich, D. G. Blair, and R. R. Burman, Why are supernovae in our Galaxy so frequent?, Mon. Not. R. Astron. Soc. **302**, 693 (1999).
[16] N. Vranesevic *et al.*, Pulsar birthrate from Parkes multi-beam survey, in *IAU Symposium 218: Young Neutron Stars and Their Environment Sydney, Australia, 2003* [*Astrophys. J.* 617, L139 (2004)].
[17] C.-A. Faucher-Giguere and V. M. Kaspi, Birth and evolution of isolated radio pulsars, Astrophys. J. **643**, 332 (2006).
[18] D. R. Lorimer *et al.*, The Parkes multibeam pulsar survey: VI. Discovery and timing of 142 pulsars and a Galactic population analysis, Mon. Not. R. Astron. Soc. **372**, 777 (2006).
[19] E. F. Keane and M. Kramer, On the birthrates of Galactic neutron stars, Mon. Not. R. Astron. Soc. **391**, 2009 (2008).
[20] I. Cholis, T. Karwal, and M. Kamionkowski, Features in the spectrum of cosmic-ray positrons from pulsars, Phys. Rev. D **97**, 123011 (2018).
[21] D. Malyshev, I. Cholis, and J. Gelfand, Pulsars versus dark matter interpretation of ATIC/PAMELA, Phys. Rev. D **80**, 063005 (2009).
[22] D. Grasso *et al.* (Fermi-LAT), On possible interpretations of the high energy electron-positron spectrum measured by the Fermi Large Area Telescope, Astropart. Phys. **32**, 140 (2009).
[23] L. Accardo *et al.* (AMS), High Statistics Measurement of the Positron Fraction in Primary Cosmic Rays of 0.5–500 GeV with the Alpha Magnetic Spectrometer on the International Space Station, Phys. Rev. Lett. **113**, 121101 (2014).
[24] AMS-02 Collaboration, AMS days at La Palma, La Palma, Canary Islands, Spain (2018), http://www.iac.es/congreso/AMSLaPalma2018/.
[25] J. Chang *et al.* (DAMPE), The DArk Matter Particle Explorer mission, Astropart. Phys. **95**, 6 (2017).
[26] G. Ambrosi *et al.* (DAMPE), Direct detection of a break in the teraelectronvolt cosmic-ray spectrum of electrons and positrons, Nature (London) **552**, 63 (2017).
[27] O. Adriani *et al.*, The CALorimetric Electron Telescope (CALET) for high-energy astroparticle physics on the International Space Station, J. Phys. Conf. Ser. **632**, 012023 (2015).
[28] O. Adriani *et al.* (CALET), Energy Spectrum of Cosmic-Ray Electron and Positron from 10 GeV to 3 TeV Observed with the Calorimetric Electron Telescope on the International Space Station, Phys. Rev. Lett. **119**, 181101 (2017).
[29] O. Adriani *et al.*, Extended Measurement of the Cosmic-Ray Electron and Positron Spectrum from 11 GeV to 4.8 TeV with the Calorimetric Electron Telescope on the International Space Station, Phys. Rev. Lett. **120**, 261102 (2018).
[30] D. R. Lorimer, The galactic population and birth rate of radio pulsars, in *IAU Symposium 218: Young Neutron Stars and Their Environment Sydney, Australia, 2003* [*IAU Symp.* 218, 105 (2004)].
[31] I. Yusifov and I. Kucuk, Revisiting the radial distribution of pulsars in the galaxy, Astron. Astrophys. **422**, 545 (2004).
[32] T. M. Tauris and R. N. Manchester, On the evolution of pulsar beams, Mon. Not. R. Astron. Soc. **298**, 625 (1998).
[33] R. N. Manchester *et al.*, The Parkes Multibeam Pulsar Survey. 1. Observing and data analysis systems, discovery and timing of 100 pulsars, Mon. Not. R. Astron. Soc. **328**, 17 (2001).
[34] G. Hobbs, D. R. Lorimer, A. G. Lyne, and M. Kramer, A Statistical study of 233 pulsar proper motions, Mon. Not. R. Astron. Soc. **360**, 974 (2005).
[35] R. N. Manchester and J. H. Taylor, *Pulsars* (Freeman, San Francisco, 1977).
[36] A. G. Lyne, R. S. Pritchard, and F. Graham-Smith, Twenty-three years of crab pulsar rotational history, Mon. Not. R. Astron. Soc. **265**, 1003 (1993).
[37] C. Gouiffes, J. P. Finley, and H. Oegelman, Rotational parameters of PSR 0540 − 69 as measured at optical wavelengths, Astrophys. J. **394**, 581 (1992).
[38] M. A. Livingstone, V. M. Kaspi, and F. P. Gavriil, Long-term phase-coherent x-ray timing of PSR B0540 − 69, Astrophys. J. **633**, 1095 (2005).
[39] A. G. Lyne, R. S. Pritchard, F. Graham-Smith, and F. Camilo, Very low braking index for the Vela pulsar, Nature (London) **381**, 497 (1996).
[40] F. Camilo, V. M. Kaspi, A. G. Lyne, R. N. Manchester, J. F. Bell, N. D'Amico, N. P. F. McKay, and F. Crawford, Discovery of two high-magnetic-field radio pulsars, Astrophys. J. **541**, 367 (2000).
[41] V. M. Kaspi, R. N. Manchester, B. Siegman, S. Johnston, and A. G. Lyne, On the spin-down of PSR B1509 − 58, Astrophys. J. Lett. **422**, L83 (1994).
[42] M. A. Livingstone, V. M. Kaspi, F. P. Gavriil, and R. N. Manchester, 21 years of timing PSR B1509 − 58, Astrophys. J. **619**, 1046 (2005).
[43] C. M. Espinoza, A. G. Lyne, and B. W. Stappers, New long-term braking index measurements for glitching pulsars using a glitch-template method, Mon. Not. R. Astron. Soc. **466**, 147 (2017).
[44] F. E. Marshall, L. Guillemot, A. K. Harding, P. Martin, and D. A. Smith, A New, low Braking Index for the lmc Pulsar B0540 − 69, Astrophys. J. **827**, L39 (2016).
[45] R. F. Archibald *et al.*, A high braking index for a pulsar, Astrophys. J. **819**, L16 (2016).
[46] S. Johnston and A. Karastergiou, Pulsar braking and the P-$\dot{P}$ diagram, Mon. Not. R. Astron. Soc. **467**, 3493 (2017).
[47] R. N. Manchester, G. B. Hobbs, A. Teoh, and M. Hobbs, The Australia Telescope National Facility pulsar catalogue, Astron. J. **129**, 1993 (2005).
[48] ATNF Catalogue website, http://www.atnf.csiro.au/research/pulsar/psrcat.
[49] M. J. Rees and J. E. Gunn, The origin of the magnetic field and relativistic particles in the Crab Nebula, Mon. Not. R. Astron. Soc. **167**, 1 (1974).
[50] J. Arons and E. T. Schrlemann, Pair formation above pulsar polar caps: Structure of the low altitude acceleration zone, Astrophys. J. **231**, 854 (1979).

[51] K. S. Cheng, C. Ho, and M. A. Ruderman, Energetic radiation from rapidly spinning pulsars. 1. Outer magnetosphere gaps. 2. Vela and Crab, Astrophys. J. **300**, 500 (1986).
[52] J. K. Daugherty and A. K. Harding, Gamma-ray pulsars: Emission from extended polar cap cascades, Astrophys. J. **458**, 278 (1996).
[53] I. Contopoulos, D. Kazanas, and C. Fendt, The axisymmetric pulsar magnetosphere, Astrophys. J. **511**, 351 (1999).
[54] S. S. Komissarov, Simulations of axisymmetric magnetospheres of neutron stars, Mon. Not. R. Astron. Soc. **367**, 19 (2006).
[55] A. Gruzinov, The Power of Axisymmetric Pulsar, Phys. Rev. Lett. **94**, 021101 (2005).
[56] I. Contopoulos and A. Spitkovsky, Revised pulsar spin-down, Astrophys. J. **643**, 1139 (2006).
[57] A. Spitkovsky, Time-dependent force-free pulsar magnetospheres: Axisymmetric and oblique rotators, Astrophys. J. **648**, L51 (2006).
[58] A. K. Harding, J. V. Stern, J. Dyks, and M. Frackowiak, High-altitude emission from pulsar slot gaps: The Crab pulsar, Astrophys. J. **680**, 1378 (2008).
[59] C. Kalapotharakos and I. Contopoulos, Three-dimensional numerical simulations of the pulsar magentoshere: Preliminary results, Astron. Astrophys. **496**, 495 (2009).
[60] K. P. Watters, R. W. Romani, P. Weltevrede, and S. Johnston, An atlas for interpreting gamma-ray pulsar light curves, Astrophys. J. **695**, 1289 (2009).
[61] X.-N. Bai and A. Spitkovsky, Modeling of gamma-ray pulsar light curves with force-free magnetic field, Astrophys. J. **715**, 1282 (2010).
[62] R. Bühler and R. Blandford, The surprising Crab pulsar and its nebula: A review, Rep. Prog. Phys. **77**, 066901 (2014).
[63] B. Cerutti, A. Philippov, K. Parfrey, and A. Spitkovsky, Particle acceleration in axisymmetric pulsar current sheets, Mon. Not. R. Astron. Soc. **448**, 606 (2015).
[64] P. Goldreich and W. H. Julian, Pulsar electrodynamics, Astrophys. J. **157**, 869 (1969).
[65] M. Hoshino, J. Arons, Y. A. Gallant, and A. B. Langdon, Relativistic magnetosonic shock waves in synchrotron sources—Shock structure and nonthermal acceleration of positrons, Astrophys. J. **390**, 454 (1992).
[66] Y. Lyubarsky and J. G. Kirk, Reconnection in a striped pulsar wind, Astrophys. J. **547**, 437 (2001).
[67] Y. E. Lyubarsky, The termination shock in a striped pulsar wind, Mon. Not. R. Astron. Soc. **345**, 153 (2003).
[68] L. Sironi and A. Spitkovsky, Acceleration of particles at the termination shock of a relativistic striped wind, Astrophys. J. **741**, 39 (2011).
[69] L. Sironi and A. Spitkovsky, Relativistic reconnection: An efficient source of non-thermal particles, Astrophys. J. **783**, L21 (2014).
[70] S. Zenitani and M. Hoshino, The generation of nonthermal particles in the relativistic magnetic reconnection of pair plasmas, Astrophys. J. **562**, L63 (2001).
[71] O. Kargaltsev, B. Cerutti, Y. Lyubarsky, and E. Striani, Pulsar-wind nebulae: Recent progress in observations and theory, Space Sci. Rev. **191**, 391 (2015).
[72] M. F. Bietenholz, N. Kassim, D. A. Frail, R. A. Perley, W. C. Erickson, and A. R. Hajian, The radio spectral index of the crab nebula, Astrophys. J. **490**, 291 (1997).
[73] J. P. Halpern and M. Ruderman, Soft X-ray properties of the Geminga pulsar, Astrophys. J. **415**, 286 (1993).
[74] J. M. Fierro, P. F. Michelson, P. L. Nolan, and D. J. Thompson, Phase-resolved studies of the high-energy gamma-ray emission from the Crab, Geminga, and VELA pulsars, Astrophys. J. **494**, 734 (1998).
[75] D. J. Thompson, Gamma radiation from psr b1055-52, Astrophys. J. **516**, 297 (1999).
[76] A. M. Atoyan, Radio spectrum of the crab nebula as an evidence for fast initial spin of its pulsar, Astron. Astrophys. **346**, L49 (1999).
[77] L. Kuiper, W. Hermsen, G. Cusumano, R. Diehl, V. Schönfelder, A. Strong, K. Bennett, and M. L. McConnell, The Crab pulsar in the 0.75–30 MeV range as seen by CGRO COMPTEL. A coherent high-energy picture from soft X-rays up to high-energy gamma-rays, Astron. Astrophys. **378**, 918 (2001).
[78] A. A. Abdo *et al.* (Fermi Pulsar Timing Consortium, Fermi-LAT), Fermi large area telescope observations of the Crab pulsar and nebula, Astrophys. J. **708**, 1254 (2010).
[79] A. A. Abdo *et al.* (Fermi-LAT), The Vela Pulsar: Results from the first year of Fermi LAT observations, Astrophys. J. **713**, 154 (2010).
[80] A. A. Abdo *et al.* (Fermi-LAT), The second Fermi Large Area Telescope Catalog of gamma-ray pulsars, Astrophys. J. Suppl. Ser. **208**, 17 (2013).
[81] R. Trotta, G. Johannesson, I. V. Moskalenko, T. A. Porter, R. Ruiz de Austri, and A. W. Strong, Constraints on cosmic-ray propagation models from a global Bayesian analysis, Astrophys. J. **729**, 106 (2011).
[82] I. Cholis, D. Hooper, and T. Linden, A predictive analytic model for the solar modulation of cosmic rays, Phys. Rev. D **93**, 043016 (2016).
[83] L. J. Gleeson and W. I. Axford, Solar modulation of Galactic cosmic rays, Astrophys. J. **154**, 1011 (1968).
[84] ACE Science Center website, http://www.srl.caltech.edu/ACE/ASC/.
[85] WSO title angles webpage, http://wso.stanford.edu/Tilts.html.
[86] S. Profumo, Dissecting cosmic-ray electron-positron data with Occam's Razor: The role of known Pulsars, Central Eur. J. Phys. **10**, 1 (2011).
[87] I. Cholis and D. Hooper, Dark matter and pulsar origins of the rising cosmic ray positron fraction in light of new data from AMS, Phys. Rev. D **88**, 023013 (2013).
[88] T. Linden and S. Profumo, Probing the pulsar origin of the anomalous positron fraction with AMS-02 and atmospheric Cherenkov telescopes, Astrophys. J. **772**, 18 (2013).
[89] P.-F. Yin, Z.-H. Yu, Q. Yuan, and X.-J. Bi, Pulsar interpretation for the AMS-02 result, Phys. Rev. D **88**, 023001 (2013).
[90] T. Linden, Circular polarization of pulsar wind nebulae and the cosmic-ray positron excess, Astrophys. J. **799**, 200 (2015).
[91] Q. Yuan *et al.*, Interpretations of the DAMPE electron data, arXiv:1711.10989.
[92] K. Fang, X.-J. Bi, and P.-F. Yin, Explanation of the knee-like feature in the DAMPE cosmic $e^- + e^+$ energy spectrum, Astrophys. J. **854**, 57 (2018).
[93] C. Evoli, T. Linden, and G. Morlino, Self-Generated Cosmic-Ray Confinement in TeV Halos: Implications for TeV Gamma-Ray Emission and the Positron Excess, arXiv:1807.09263.